Application of two-phase transition model in underwater explosion cavitation based on compressible multiphase flows

Cite as: AIP Advances 12, 025209 (2022); doi: 10.1063/5.0077517
Submitted: 3 November 2021 • Accepted: 18 January 2022 •
Published Online: 8 February 2022

Jun Yu (余俊),[a] Jian-hu Liu (刘建湖), Hai-kun Wang (王海坤), Jun Wang (汪俊), Zhang-tao Zhou (周章涛), and Hai-bin Mao (毛海斌)

AFFILIATIONS

China Ship Scientific Research Center, Wuxi 214082, China

[a]Author to whom correspondence should be addressed: yujun@cssrc.com.cn

ABSTRACT

Underwater explosion cavitation is generally simulated using a one-fluid model based on compressible multicomponent flows. Owing to the lack of mass and heat transfer between liquid and vapor phases, this model is incapable of extensively analyzing the cavitation mechanism in underwater explosion. In this study, we extend the phase transition model provided by Chiapolino *et al.* to the field of underwater explosion cavitation. The model presents a more accurate description of the thermodynamics of cavitation processes involving liquid–vapor phase transition. The numerical results show that the phase transition exhibits significant potential in the study of underwater explosion cavitation, and the likely occurrence of creation, development, and collapse of the cavitation can be captured. A vortex band composed of a large number of tiny cavitation bubbles can be observed in the numerical results, which is consistent with the experiment in underwater explosion near a free surface. The variation range of the cavitation domain calculated by the phase transition model is basically consistent with the experiment, which proves the reliability and accuracy of the calculation model. Meanwhile, the distribution characteristics of quantities such as density, pressure, and vapor phase volume fraction in the cavitation domain can be effectively obtained in simulation, which are usually difficult to capture in experiments. The creation mechanism of cavitation near a free surface and rigid wall is different. However, the collapse mechanism is similar. The results of this study could provide an in-depth understanding of the dynamic behavior of cavitation in underwater explosion.

I. INTRODUCTION

Phase transition between liquid and vapor phases is a well-established phenomenon, which occurs in nature and many engineering applications such as flows around ships or submarine propellers. When the underwater explosion (UNDEX) shock wave reaches the free surface or structure surface, the air–water interface and structure movement can lead to rarefaction wave occurrence, which can easily induce cavitation phenomena.[1,2] For such cavitation flows, the pressure caused by cavitation collapse is a major concern in engineering. Therefore, the need to understand the basic mechanisms that contribute to cavitation evolvement has attracted extensive research on cavitation flows. Both experimental and numerical studies have been conducted to investigate such cavitation phenomena. However, conducting an experimental study can be challenging owing to the increase in precision requirements and complexity of cavitation problems in engineering. As a result, numerical simulation has attracted much attention in the past few decades. The cavitation model has been developed for more than half a century owing to the complex interactions between multiphase flows.

Cavitation models in the field of compressible fluids are mainly divided into two categories. The first is one-fluid cavitation model.[3–5] This model assesses the liquid and vapor phases using average state quantity. The earliest one-fluid model used extensively in UNDEX is the cut-off model.[5] In this model, the pressure is equal to the given value once the flow pressure is detected to be lower than the saturated pressure. Phase transition between the liquid and vapor

phases is not considered in this model. Moreover, the treatment of unifying the internal cavitation domain to a given saturated pressure can destroy the conservation of fluid motion. The vacuum model is another type of one-fluid model. This model is mathematically sound; however, it is difficult to extend to multi-dimensions.[6] Liu *et al.*[4] proposed an isentropic one-fluid model, which treated the fluid as a homogeneous mixture comprising isentropic vapor and liquid phases. The Schmidt model is also an important model, which was used to efficiently simulate cavitation flow occurring in high pressure and high velocity nozzles.[7] However, it cannot be extended to the simulation of a large-scale unsteady cavitation with a large vapor to liquid density ratio, which is easy to produce "saturated" pressure that is significantly higher than physical saturated pressure. Xie *et al.*[8] made some improvement on the application of the Schmidt model in unsteady transient cavitation flow and proposed the modified Schmidt model to ameliorate this problem. Daramizadeh and Ansari[9] adopted a reduced five-equation model to simulate underwater explosion cavitation using a new isentropic cavitation model. Some one-fluid models, owing to their simplicity and efficiency, have been embedded in commercial software programs, such as LS-DYNA, MSC.DYTRAN, ABAQUS, and AUTODYN. These models are also used to predict the starting time and simple evolution process of the cavitation domain in engineering without high precision requirements. However, they are unable to predict and analyze the mechanism of mass and heat conversion between liquid and vapor phases in cavitation flow because of the assumption of homogeneity in the cavitation domain and no phase transition between liquid and vapor phases.

The second model is the two-fluid cavitation model, which has been used by researchers, such as Le Métayer *et al.*,[10–12] Saurel *et al.*,[13] and Pelanti and Shyue.[14] Thermal and chemical relaxation effects due to mass and heat conversion between liquid and vapor phases are considered in this model. Therefore, new relaxation source terms associated with heat and mass transfer appear in the governing equations. Saurel *et al.*[13] and Zein *et al.*[15] directly integrated these ordinary differential equations (ODEs), which required a diminutive time step for stability because of the stiffness of the chemical relaxation terms. Pelanti and Shyue employed phasic total energy equations instead of the phasic internal energy equations of the classical 6-equation system.[14] Temperature and Gibbs free energy exchange terms were included in the equations as relaxation terms to model heat and mass transfer and subsequently liquid–vapor transition. This method influenced the development of the cavitation phase transition model based on thermodynamic equilibrium, which provides important support for the study of the essential characteristics of cavitation. Subsequently, Pelanti and Shyue extended the model to multiphase fluids involving the liquid and vapor phases of one species and a third inert gaseous phase.[16] In the study, a cylindrical underwater explosion was simulated near the rigid wall and free surface, and the occurrence of creation and collapse of vapor cavities in the liquid region were captured. The study is generally acknowledged as the first to apply the two-fluid phase transition model to the field of underwater explosion cavitation. Owing to the complex computation formulas and complicated calculation programs in the six-equation system, Chiapolino *et al.*[17] established the phase transition model based on the four-equation system, in which the thermodynamic equilibrium conditions were used to reduce and approximate the solution of the ODE relaxation term to the solution of a simple system of algebraic equations. On the basis of this new phase transition relaxation algorithm, Chiapolino *et al.*[18] proposed a simple and fast method to treat thermodynamic equilibrium between liquid and vapor phases instead of the iterative procedures in the four-equation model and also allow over 50% systematic CPU saving without compromising accuracy. However, in some of our test examples, the simple and fast solver produced negative pressure or internal energy in the phase transition relaxation without a special treatment. Zhang proposed a two-phase flow model for liquid–vapor phase transition in cavitating flows based on the five-equation system using temperature and chemical relaxation with the monotonic mixture speed of sound.[19] Compared with Chiapolino model,[18] the interface advection equation was non-conservative and could not contain other fluid components in the Zhang model.[19]

Generally, the one-fluid model has been extensively used in underwater explosion cavitation than the two-fluid model. However, owing to its inability to track the convection and phase transition between liquid and gas phases, the one-fluid model is limited in the study of occurrences of creation, evolution, and collapse mechanism in underwater explosion cavitation. The development of cavitation in underwater explosion has a significant impact on the shock wave propagation, bubble movement, and structure damage. Therefore, it is necessary to extensively study the cavitation phenomena in underwater explosion. The two-fluid model describes the convection and transition process between the liquid and vapor phases based on thermodynamics, which is similar to the essential mechanism of cavitation. Therefore, it is widely applied in the study of underwater explosion cavitation. In this study, a two-fluid model developed by Chiapolino *et al.*[18] has been adopted for compressible multiphase fluids, and some interesting phenomena are obtained. The remainder of this paper is as follows: The four-equation model with phase transition relaxation and the numerical methods with mixture sound speed and HLLC Riemann solver are presented in Secs. II and III, respectively. Several numerical examples are given in Secs. IV A–IV C. Two-dimensional vapor bubble compression and collapse are presented in Sec. IV D, and two cavitation phenomena are shown in Sec. IV E. Finally, discussions and conclusions are drawn in Sec. V.

II. CONTROL EQUATIONS WITH PHASE TRANSITION RELAXATION

A. Compressible multiphase model without phase transition

Under the assumption of no phase transition, the governing equations for multiphase compressible flow without viscous and thermal effects are as follows:

$$\begin{cases} \dfrac{\partial \rho}{\partial t} + \nabla \cdot (\rho \mathbf{u}) = 0, \\ \dfrac{\partial (\rho \mathbf{u})}{\partial t} + \nabla \cdot (\rho \mathbf{u} \otimes \mathbf{u} + p\mathbf{I}) = 0, \\ \dfrac{\partial (\rho E)}{\partial t} + \nabla \cdot ((\rho E + p)\mathbf{u}) = 0, \\ \dfrac{\partial \rho Y_k}{\partial t} + \nabla \cdot (\rho Y_k \mathbf{u}) = 0, \end{cases} \tag{1}$$

where ρ, p, $\mathbf{u}$, and E account for the density, pressure, velocity vector, and total energy per unit mass, respectively. Y_k is the mass fraction of the kth phase fluid, which can be specified as follows: $k = 1$ for the liquid phase, $k = 2$ for the vapor phase, and $k = 3, \ldots, N$ for the other non-condensable gaseous or liquid phases. In this paper, Y_3 denotes the mass fraction of air and Y_4 denotes the mass fraction of explosion gas.

B. System closure

The closure of the four-equation model is achieved using an equation of state (EOS). In this model, both liquid and vapor phases require a personalized EOS, with parameters carefully chosen to fit the phase diagram. To facilitate the solution of the governing equations, it is generally necessary to use the same type of EOS for the liquid and vapor phases. The building of such an EOS has been addressed by Le Métayer *et al.*[10] on the basis of the stiffened gas (SG) EOS. Additionally, the same authors proposed an improved formulation Noble-Abel Stiffened-Gas (NASG) EOS, which substantially improves liquid specific volume accuracy by considering the repulsive molecular effects in addition to those existing in the SG EOS (agitation and attraction).[18,20] The main formulas for the NASG EOS are given by the following equations:

$$\begin{cases} p_k(v_k, e_k) = \dfrac{(\gamma_k - 1)(e_k - q_k)}{v_k - b_k} - \gamma_k p_k^{\infty}, \\ T_k(p_k, v_k) = \dfrac{(p_k - p_k^{\infty})(v_k - b_k)}{(r_k - 1)C_{\mathrm{v,k}}}, \\ g_k(p_k, T_k) = \left(\gamma_k C_{\mathrm{v},k} - q_k'\right)T_k - C_{\mathrm{v},k}T_k \ln \dfrac{T_k^{\gamma_k}}{\left(p_k + p_k^{\infty}\right)^{\gamma_k - 1}} + b_k p_k + q_k, \\ c_k(p_k, v_k) = \sqrt{\dfrac{\gamma_k v_k^2 \left(p_k + p_k^{\infty}\right)}{v_k - b_k}}, \end{cases} \tag{2}$$

where e, T, c, g, and $v = 1/\rho$ account for the internal energy, temperature, sound speed, Gibbs free energy, and specific volume, respectively. The Gibbs free energy is obtained using $g = h - Ts$, with h and s being the enthalpy and entropy, respectively. Here, C is the phase specific heat at constant volume and b represents the covolume of the fluid. Parameters $\gamma_k, p_k^{\infty}, q_k, q_k'$ are the constant coefficient characteristics of the thermodynamic properties of the fluid. For the properties of the thermodynamic nature of the NASG equation of state, refer to Ref. 20. As shown in the study by Saurel *et al.*,[21] it is convenient to obtain these parameters once the saturation curves $[p_{sat}(T), v_{g,sat}(T), v_{l,sat}(T), h_{g,sat}(T)$, and $h_{l,sat}(T)]$ are known. The formulas of internal energy, specific volume, entropy, and temperature are obtained using a simple transformation of Eq. (2) as follows:

$$\begin{cases} e_k(p_k, T_k) = \dfrac{p_k + \gamma_k p_k^{\infty}}{p_k + p_k^{\infty}} C_{\mathrm{v},k} T_k + q_k, \\ v_k(p_k, T_k) = \dfrac{T_k C_{\mathrm{v},k}(\gamma_k - 1)}{p_k + p_k^{\infty}} + b_k, \\ s_k(p_k, T_k) = C_{\mathrm{v},k} \ln \dfrac{T_k^{\gamma_k}}{\left(p_k + p_k^{\infty}\right)^{\gamma_k - 1}} + q'_k, \\ T_k(e_k, p_k) = \dfrac{(e_k - q_k)(p_k + p_k^{\infty})}{C_{\mathrm{v},k}\left(p_k + \gamma_k p_k^{\infty}\right)}. \end{cases} \tag{3}$$

TABLE I. NASG coefficients for liquid water, water vapor, and air.

Coefficients	Liquid water	Water vapor	Air
C_p(J/kg/K)	4 285	1 401	1007
C_v(J/kg/K)	3 610	955	719
γ	1.19	1.47	1.4
P_∞(Pa)	7.028×10^8	0	0
q(J/kg)	−1177 788	2 077 616	0
q'(J/kg/K)	0	14 317	0
$b\left(\mathrm{m}^3/\mathrm{kg}\right)$	6.61×10^{-4}	0	0
W(g/mol)	18	18	29

Based on the assumption that the Gibbs free energy of the liquid phase is equal to that of the vapor phase in the equilibrium state, the following formula can be obtained:

$$\ln(p_{sat} + p_2^{\infty}) = A + \frac{B + E \cdot p_{sat}}{T_{sat}} + C \cdot \ln(T_{sat}) + D \cdot \ln(p_{sat} + p_1^{\infty}), \tag{4}$$

with

$$A = \frac{C_{p,1} - C_{p,2} + q'_2 - q'_1}{C_{p,2} - C_{v,2}}, \quad B = \frac{q_1 - q_2}{C_{p,2} - C_{v,2}}, \quad C = \frac{C_{p,2} - C_{p,1}}{C_{p,2} - C_{v,2}}, \quad D = \frac{C_{p,1} - C_{v,1}}{C_{p,2} - C_{v,2}}, \quad E = \frac{b_1 - b_2}{C_{p,2} - C_{v,2}}, \tag{5}$$

where $C_{p,k}$ denotes the heat capacity at constant pressure for the phase k, $C_{p,k} = \gamma_k C_{v,k}$.

For liquid water and its steam, the NASG parameters determined in the [273–500] K temperature range are given in Table I.[20]

C. Phase transition model

Although the solution from Eq. (1) satisfies the pressure and temperature equilibrium between individual phases in the mixture, it is not guaranteed to satisfy the conditions of saturated pressure and temperature (p, T) between the liquid and vapor phases as in Eq. (4). Therefore, it is necessary to introduce the phase transition model to ensure that the final equilibrium state (p^*, T^*) is saturated at each step as shown in Fig. 1.

During the phase transition process, the mixture mass and internal energy remain constant. Therefore, the thermal and chemical relaxation can be done by enforcing the mechanical, thermal, and chemical equilibrium conditions as

$$\begin{cases} T = T_k, p = p_k, \forall k, \\ g_1 = g_2, v = \sum_{k=1}^{N} Y_k v_k, e = \sum_{k=1}^{N} Y_k e_k. \end{cases} \tag{6}$$

As mentioned in Ref. 18, the ideal mixture model of Dalton's law and separate chemical species are equivalent when the fluids are ideal gases evolving in both temperature and pressure equilibrium. Therefore, the vapor partial pressure is directly proportional to the vapor molar fraction,

$$p_{partial} = \frac{Y_2^*/W_2}{Y_2^*/W_2 + \sum_{3}^{N} Y_k/W_k} p^* = p_{sat}\left(T^*\right), \tag{7}$$

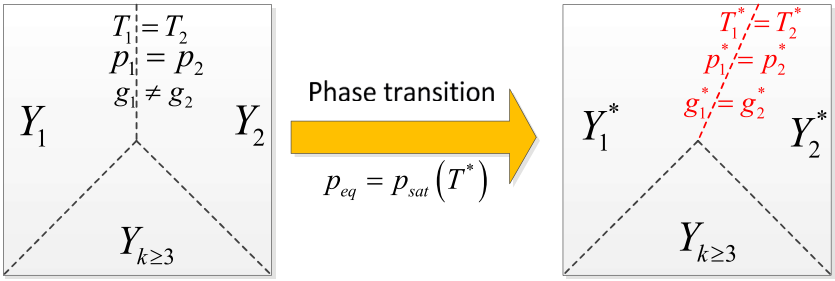

FIG. 1. Schematic diagram of mass fraction distribution of different phases in fluid before and after phase transition treatment. The dotted lines represent the location of the volume division boundary.

where W_k is the molar mass of species k and the superscript "*" denotes the finial state. Therefore, the following system has to be solved:

$$\begin{cases} p_{partial} = \dfrac{Y_2^*/W_2}{Y_2^*/W_2 + \sum_3^N Y_k/W_k} p^* = p_{sat}(T^*), \\ v = Y_1^* v_1(T^*, p^*) + Y_2^* v_2(T^*, p^*) + \sum_{k=3}^N Y_k v_k(T^*, p^*), \\ e = Y_1^* e_1(T^*, p^*) + Y_2^* e_2(T^*, p^*) + \sum_{k=3}^N Y_k e_k(T^*, p^*), \\ \ln(p^* + p_2^\infty) = A + \dfrac{B + E \cdot p^*}{T^*} + C \cdot \ln(T^*) + D \cdot \ln(p^* + p_1^\infty). \end{cases} \tag{8}$$

This system contains four unknown variables with four equations, which can be solved by the Newton iterative method.

III. NUMERICAL METHOD

The control equation (1) is strictly conservative in divergence form and can be solved using the reconstruction-and-evolve strategy in a finite volume formulation.[22] The reconstructions are addressed with the monotonic upwind scheme for conservation laws (MUSCL) method using the van Leer slope limiter. The numerical fluxes are built using the HLLC approximate Riemann solver.[23] Here, we focus on the choice of sound speed in the mixture and the construction of the HLLC solver, a solver based on ordinary Euler equations.

A. Speed of sound for the estimates of wave speed in the HLLC solver

The estimation of wave speed on both sides of the element boundary is an important part in HLLC solver construction. This is because the solver reconstruction can affect the accuracy of flux solution. The Wood speed[24] of sound is widely used in the multicomponent flow model.[25–27] Based on a previous study,[28] the Wood speed of sound does suffer from the known numerical issue of nonmonotonic behavior within the material interface. This limitation led to the development of the six-equation model by Saurel *et al.*,[28] after which a monotonic frozen speed of sound $c_{eq}^2 = Y_1 c_1^2 + Y_2 c_2^2$ (subsequently adopted in Ref. 14) was proposed. Another model for the monotonic speed of sound, known as the five-equation model, was built by Allaire *et al.*[29] The Allaire speed with the mixture NASG EOS can be described as

$$c_{eq}^2 = \frac{\sum_k y_k \xi_k c_k^2}{\xi}, \tag{9}$$

with

$$\begin{cases} \xi_k = \left(\dfrac{\partial \rho_k e_k}{\partial p_k}\right)_{\rho_k} = \dfrac{1 - \rho_k b_k}{\gamma_k - 1}, \\ \delta_k = \left(\dfrac{\partial \rho_k e_k}{\partial \rho_k}\right)_{p_k} = \dfrac{-b_k(p_k + \gamma_k p_k^\infty)}{\gamma_k - 1} + q_k, \\ c_k^2 = \dfrac{(h_k - \delta_k)}{\xi_k} = \gamma_k v_k^2 \dfrac{p_k + p_k^\infty}{v_k - b_k}, \\ \xi = \sum_{k=1}^N (\phi_k \xi_k) = \sum_{k=1}^N \left(\dfrac{\rho Y_k}{\rho_k} \xi_k\right), \end{cases} \tag{10}$$

where h_k and ϕ_k denote the enthalpy per unit mass and volume fraction for the kth phase, respectively, and c_{eq} is the mixture speed of sound.

With the increase in the water vapor volume fraction at atmospheric pressure, three types of mixture sound speed models display different characteristics, as shown in Fig. 2. The Allaire speed generally shows significant monotonic behavior with the increasing gas

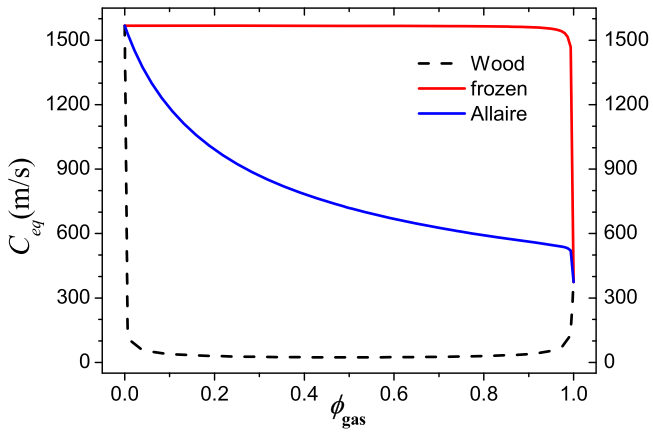

FIG. 2. Representation of the different mixture speeds of sound for the liquid water–air mixture under atmospheric conditions.

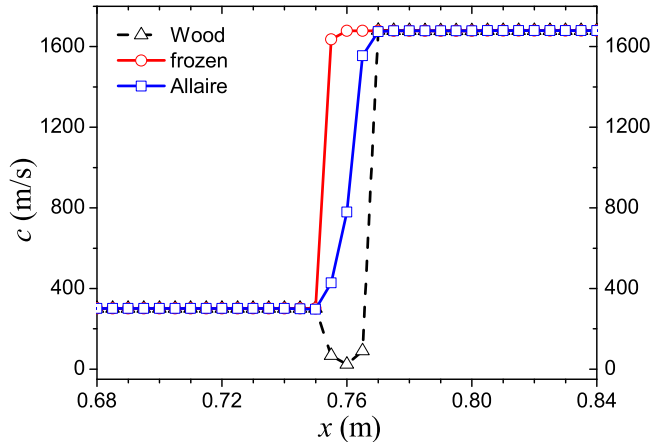

FIG. 3. Comparison of different types of mixture sound speeds during the numerical advection of the air–water interface.

volume fraction. Contrastingly, the frozen speed is basically constant in a large range; however, it changes abruptly when it is very close to the pure vapor phase. Comparatively, the non-monotonicity of the Wood speed of sound is more apparent.

The different behaviors of the above three mixture speeds in 1D are shown in Fig. 3. Air and water are separated at $x = 0.5$ m at room temperature and atmospheric pressure. The uniform velocity of the whole flow field is 100 m/s. Figure 3 shows the different mixture sound speeds at $t = 3$ ms. It can be observed that the frozen speed and Allaire speed are monotonic within the water–air interface. As stated by Perigaud and Saurel,[30] when the Wood speed is used, the speed of sound tends to be very low inside the mixture flow zone at interfaces, leading to the occurrence of sonic points without any flow acceleration. This further results in the difficult approximation of Riemann invariants and Riemann solver convergence. It can be observed that there are practically no transitional nodes at the discontinuity when frozen speed is used, which is too ideal for actual procedures. Figure 4 shows the schematic diagram of the three types of sound

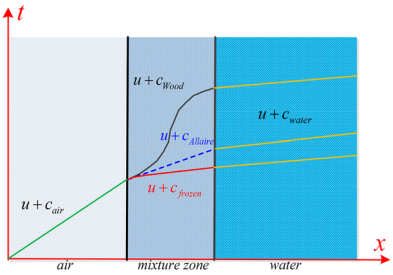

FIG. 4. Schematic representation in the (x, t) diagram of the interaction between an acoustic wave and the numerical diffusion zone of an interface computed with three types of mixture sound speeds. The blue line in the left light gray zone denotes the wave speed of pure air, and the yellow lines in the right blue zone denote the wave speed of pure water. In the middle dark gray zone, the black line, blue dotted line, and red line account for the wave speeds by Wood, Allaire, and the frozen method, respectively.

speed wave transmission through diffuse interfaces corresponding to Fig. 4. Based on the comprehensive comparison mentioned above, the Allaire speed was preferred in all the examples.

B. HLLC Riemann solver

When the numerical flux construction on the x-direction (which can be obtained in the same manner as the y-direction) is used as an example, the intercell flux of the HLLC approximate Riemann solver is given by[23]

$$F_{i+1/2}^{HLLC} = \begin{cases} F(q_L) 0 \le s_L, \\ F(q_L) - s_L\left(q_L^* - q_L\right) s_L < 0 \le s^*, \\ F(q_R) - s_R\left(q_R^* - q_R\right) s^* < 0 \le s_R, \\ F(q_R) s_R \le 0, \end{cases} \tag{11}$$

$$q_K^* = \frac{s_K - u_K}{s_K - s^*} \begin{pmatrix} \rho_K \\ \rho_K s^* \\ \rho_K v \\ \rho_K E_K + \left(s^* - u\rho_K\right)\left[\rho_K s^* + p_K/(s_K - u_K)\right] \\ \rho_K Y_{k,K} \end{pmatrix},$$
$$K = L \text{ or } R; \quad k = 1, 2, \ldots, N, \tag{12}$$

where "L" and "R" refer to the left and right states of a cell side, respectively, and k represents the individual phase. s_L and s_R are the left and right wave speeds estimated using[40]

$$s_R = \max(u_L + c_L, u_R + c_R), \quad s_L = \min(u_L - c_L, u_R - c_R). \tag{13}$$

The middle wave speed s^* is given as

$$s^* = \frac{\left(\rho u^2 + p\right)_L - \left(\rho u^2 + p\right)_R - s_L(\rho u)_L + s_R(\rho u)_R}{(\rho u)_L - (\rho u)_R - s_L\rho_L + s_R\rho_R}. \tag{14}$$

A MUSCL–Hancock method is used to increase the modeling accuracy from first order to second order.[23] The finite volume method and structured grid are adopted in numerical schemes.

C. Solution procedure

The integrated algorithm can be summarized as follows: Given all values at time step n, the values at time step n + 1 can be updated as follows:

(1) At each cell boundary, the conservative variables are reconstructed by the second order MUSCL–Hancock method using the van Leer slope limiter, while the numerical fluxes are obtained using the HLLC approximate Riemann solver.
(2) All flow variables are evolved with the Godunov type method in the homogeneous hyperbolic step, and temporary variables (v, e, p, T, and Y_k) are subsequently solved.
(3) The nonlinear system (8) is solved to obtain the equilibrium state (p^*, T^*, and $Y_{k=1,2}$) using the Newton–Raphson iterative method. It can be divided into the following situations:
    (3.1) If the liquid phase mass fraction satisfies the condition of $Y_1 < 10^{-8}$, the fluid can be

approximated as the gas mixture with overheated vapor. No phase transition occurs at this condition, and there is no need to solve the phase transition [Eq. (8)].

(3.2) Otherwise, it is necessary to use the iterative method to solve Eq. (8). The initial state can choose the solution of step (2).

(4) Step (1) is repeated, followed by the next time step.

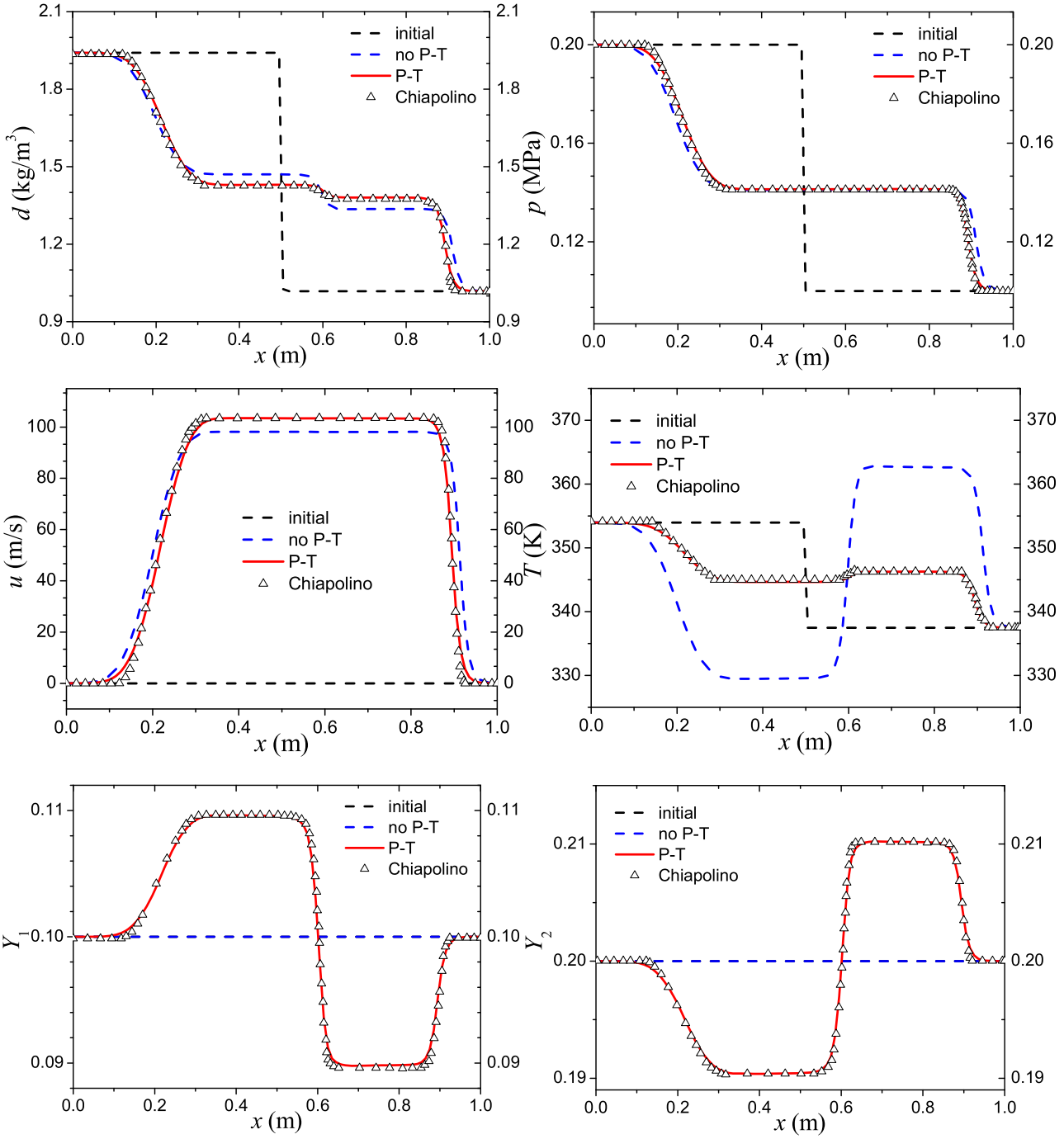

FIG. 5. Numerical results for the shock tube test with a two-phase mixture made of liquid water, vapor water, and air. The dashed black lines represent the initial conditions. The dashed blue lines represent the solutions without phase transition (no P-T). The red lines represent the solutions with phase transition (P-T). The triangle symbols represent the solutions from the study by Chiapolino *et al.*

IV. NUMERICAL RESULTS AND DISCUSSION

A. Shock tube test with a mixture far from the phase bounds

A two-phase mixture with initial mass fractions is set to $Y_1 = 0.1$ (liquid), $Y_2 = 0.2$ (vapor), and $Y_3 = 0.7$ (air). This is considered throughout the shock tube with an initial pressure ratio of two. This test has been simulated by Chiapolino *et al.*[18] The initial discontinuity is located at $x = 0.5$ m, and the initial condition is given as

$$(\rho, u, p, Y_1, Y_2, Y_3) = \begin{cases} (1.941, 0, 2\times10^5, 0.1, 0.2, 0.7), & x < 0.5, \\ (1.018, 0, 1\times10^5, 0.1, 0.2, 0.7), & x \geq 0.5. \end{cases} \tag{15}$$

The simulations are performed on meshes with 100 cells. The results are shown at time $t = 1$ ms in Fig. 5. It can be observed from the plots that there are some differences between the cases with and without phase transition. The vapor mass fraction on transition from the liquid phase to vapor phase occurs near the right shock wave front using phase transition as shown in the vapor mass fraction curve in Fig. 5, and the evaporation process induced by shock compression can be captured clearly. Meanwhile, the condensation induced by the expansion wave can be obtained as shown in the liquid mass fraction curve in Fig. 5. The numerical results with phase transition show consistency with Chiapolino's solutions.

B. Shock tube test with a mixture containing mainly liquid water

In the test, a shock tube with an initial pressure ratio of two is considered. The vapor and air mass fractions are deduced as $Y_2 = 9.453\times10^{-8}$ and $Y_3 = 10^{-5}$ in the left chamber and $Y_2 = 1.9198\times10^{-7}$ and $Y_3 = 10^{-5}$ in the right chamber. The liquid mass fraction Y_1 is obtained by $Y_1 = 1 - Y_2 - Y_3$. Because there are excessive significant digits, all the values of Y_1 shown in this paper are approximate. The initial condition is given as

$$(\rho, u, p, Y_1, Y_2, Y_3) = \begin{cases} (1051.4, 0, 2\times10^5, 0.999\,99, 9.453\times10^{-8}, 10^{-5}), & x < 0.5, \\ (1046.5, 0, 1\times10^5, 0.999\,99, 1.919\,8\times10^{-7}, 10^{-5}), & x \geq 0.5. \end{cases} \tag{16}$$

Numerical results are shown at time $t = 1.5$ ms with 200 grids in Fig. 6. Because the liquid mass fractions on both sides of the discontinuity are too close to one (the deviation is less than 10^{-8}), the ordinate coordinate of the Y_1 diagram in Fig. 6 is all shown as one. It can be observed from the temperature diagram that it is quasi-isothermal notwithstanding the slight evaporation and condensation processes appearing through the shock and rarefaction wave propagation. This example implies that the present relaxation algorithm can analyze the limiting calculation conditions in which the flows contain an extremely low mass fraction of the water vapor phase, which is essential for the simulation of cavitation in underwater explosion. According to the basic theory,[41] it is believed that the generation of cavitation (the scale visible to the naked eye) originates from the initial existence of an extremely low volume fraction of the vapor phase in water.[31]

C. Double expansion test with a two-phase mixture mainly made of liquid water

The following example simulates cavitation induced by initial subcooled water, which has also been researched by Chiapolino *et al.*[18] The initial temperature, pressure, and air mass fraction are 10^5 Pa, 293 K, and 10^{-5} throughout the entire tube, respectively. The vapor and liquid mass fractions are then set to $Y = 1.919\times10^{-7}$ and $Y \approx 0.999\,98$ in the entire tube. The initial velocity is set to −1 m/s at left and +1 m/s at right chambers. The initial condition is given as

$$(\rho, u, p, Y_1, Y_2, Y_3) = \begin{cases} (1046.5, -1, 10^5, 0.999\,99, 1.919\times10^{-7}, 10^{-5}), & x < 0.5, \\ (1046.5, 1, 10^5, 0.999\,99, 1.919\times10^{-7}, 10^{-5}), & x \geq 0.5. \end{cases} \tag{17}$$

The numerical results are shown at time $t = 3.5$ ms in Fig. 7. Although there is litter difference in terms of density, pressure, velocity, and temperature under the condition of phase transition, there will be a big difference in the vapor volume fraction. The phenomenon of vapor generation can be captured by the phase transition model in the vicinity of the discontinuity. Good agreement is again obtained between the present and Chiapolino models.

D. 2D vapor bubble compression and collapse

We aim to simulate the vapor bubble compressed by the shock wave in water, which has also been considered in Refs. 32–34. Here, a similar example with a vapor bubble of radius 0.2 m set at the location of (0.8, 0.6) in a liquid-filled chamber is shown in Fig. 8. The computational domain is $\Omega = [0, 2.0] \times [0, 1.2]$ m^2, which is discretized by 1000 × 600 uniform grids. The initial condition is

$$(\rho, u, p, Y_1, Y_2, Y_3) = \begin{cases} (1008, 0, 10^5, 0.999\,95, 10^{-6}, 5.209\times10^{-5}), & x > 0.6, \\ (1026, 87, 10^8, 0.999\,98, 10^{-8}, 1.528\times10^{-5}), & x < 0.6, \\ (0.61, 0, 10^5, 0.006\,66, 0.99, 3.373\times10^{-3}) & \textit{in cavity}. \end{cases} \tag{18}$$

Figure 9 displays the contour plots of the density, pressure, vapor mass, and volume fraction at different times of 0.40, 0.71, 0.89, 1.05, 1.09, 1.19, and 1.45 ms. It can be observed that after the circular vapor bubble is compressed by a high pressure shock wave, it begins to sag to the right and finally forms a water jet. Although the initial shock wave peak pressure is only 10^8 Pa, the maximum impact pressure induced by the water jet reaches 2.4×10^8 Pa at ~1.09 ms as shown in Fig. 9. It can be observed that no spurious pressure oscillations at the interfaces can be found, which displays that the ability of the phase transition treatment and wave propagation capture in the solver is appropriate.

E. Two cavitation phenomena in underwater explosion

Cavitation is an essential phenomenon in underwater explosion and has a significant impact on shock wave loading, bubble movement, and underwater structures. Several theories have explained

and analyzed the generation, evolution, and collapse mechanism of cavitation in underwater explosion.[35–37] There is a significant difference between theoretical and experimental results owing to the simple hypothesis in the theoretical model. Many experimental studies on underwater explosion cavitation have been conducted in the past decade. Compared with the blurred images of cavitation shown in several existing underwater explosion experiments, Cui *et al.*[38] obtained a set of clear images of cavitation near a free

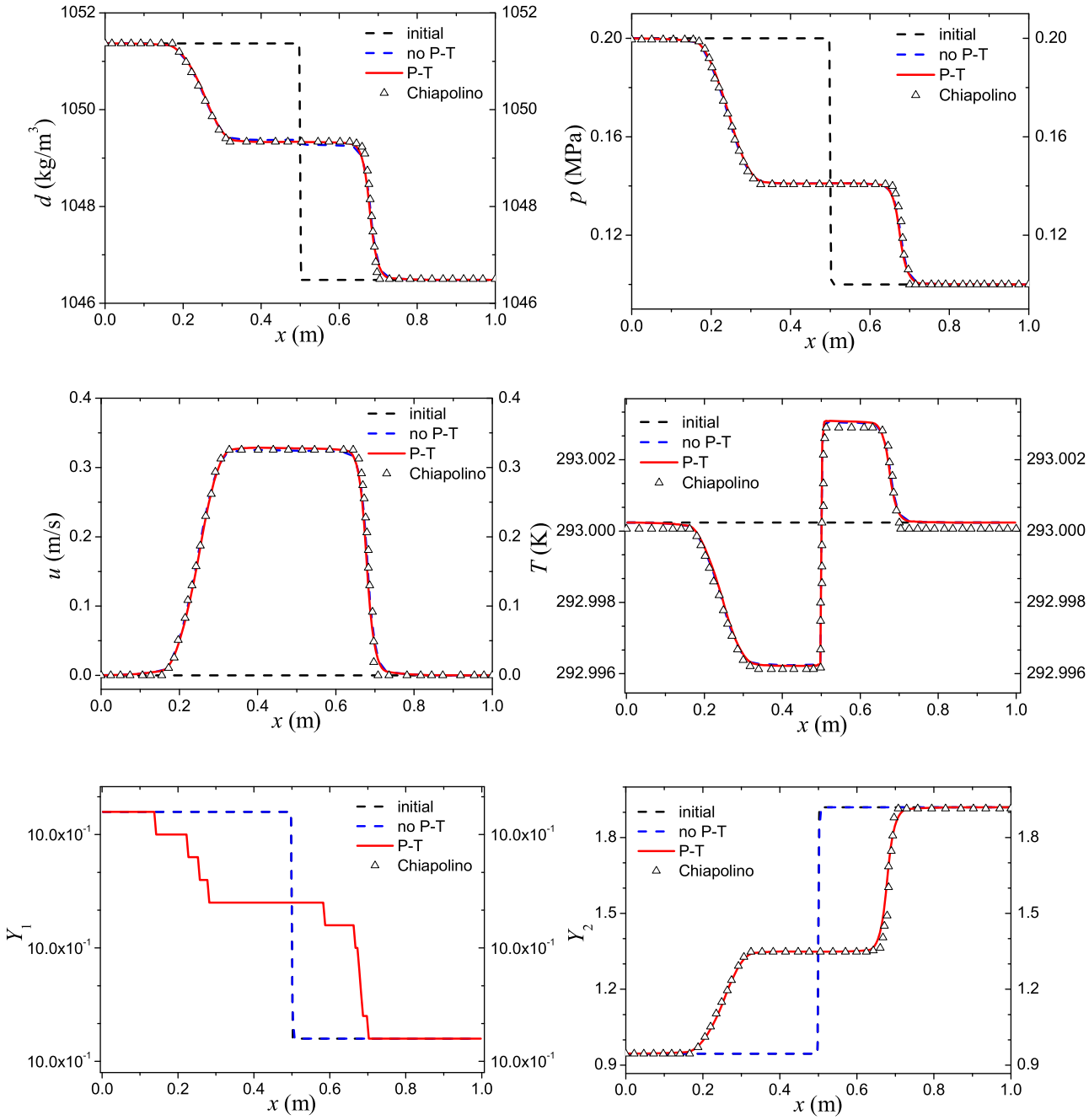

FIG. 6. Numerical results for the shock tube test with a two-phase mixture made of liquid water, vapor water, and air. The dashed black lines represent the initial conditions. The dashed blue lines represent the solutions without phase transition (no P-T). The red lines represent the solutions with phase transition (P-T). The triangle symbols represent the solutions from the study by Chiapolino *et al.*

surface while studying the influence of different boundary conditions on a small-charge underwater explosion bubble. These cavitation images provide valuable information for numerical simulation. In this study, we adopt the phase transition model based on compressible multiphase fluids to partially emerge the cavitation phenomenon near a free surface in the experiment. This is discussed in Sec. IV E 1. The cavitation near the structure in underwater explosion is also an important phenomenon, and the occurrence of

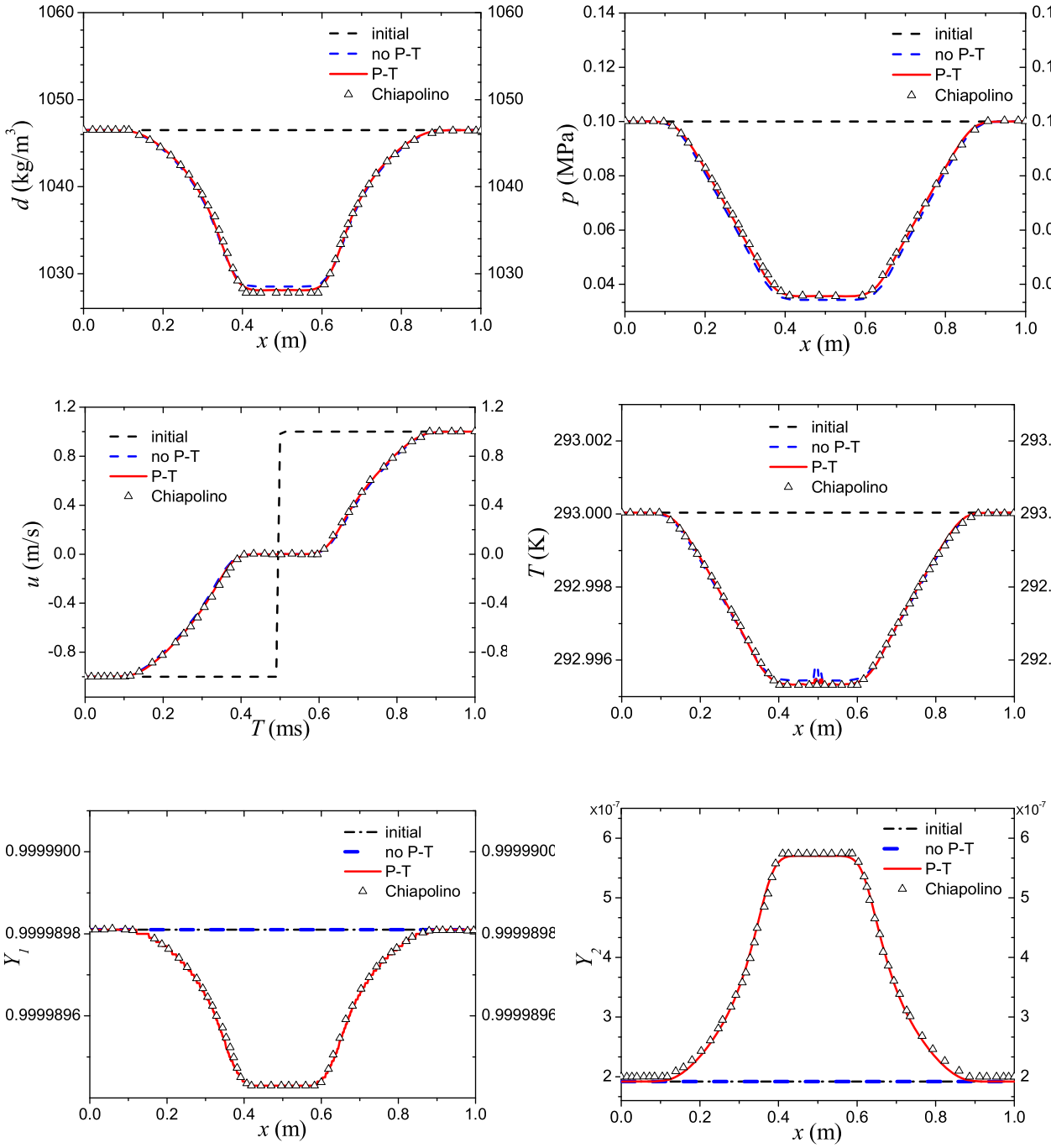

FIG. 7. Numerical results for the shock tube test with a two-phase mixture made of liquid water, vapor water, and air. The dashed black lines represent the initial conditions. The dashed blue lines represent the solutions without phase transition (no P-T). The red lines represent the solutions with phase transition (P-T). The triangle symbols represent the solutions from the study by Chiapolino *et al.*

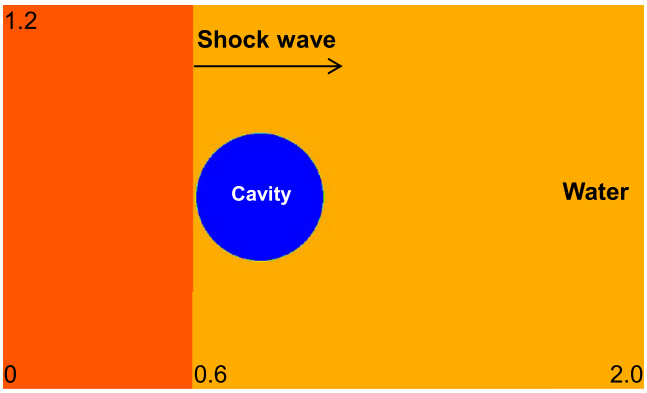

FIG. 8. Schematic of computation with the initial cavity and shock wave.

creation and collapse is dissimilar to that near a free surface. This type of cavitation near a rigid wall using a multiphase flow model is provided in Sec. IV E 2.

1. Underwater explosion cavitation near a free surface

In the experimental arrangement,[38] 4.0 g PETN (pentaerythritol tetranitrate) is detonated at a depth of 0.13 m from the free surface in a 2 × 2 × 2 m^3 cubic steel water tank filled with tap water. Its TNT (trinitrotoluene) equivalence mass is ~5.2 g. To simulate the occurrence of cavitation, a 2D axisymmetric model is used to research the 3D cavitation near a free surface. This is presented in Fig. 10. Calculations are performed on a rectangular computational domain $\Omega = [0, 1.5] \times [-1.8, 0.2]$ m^2 discretized using 600 × 800 uniform grids. The impenetrable boundary condition is applied on the symmetric axis (y-axis), and the non-reflecting

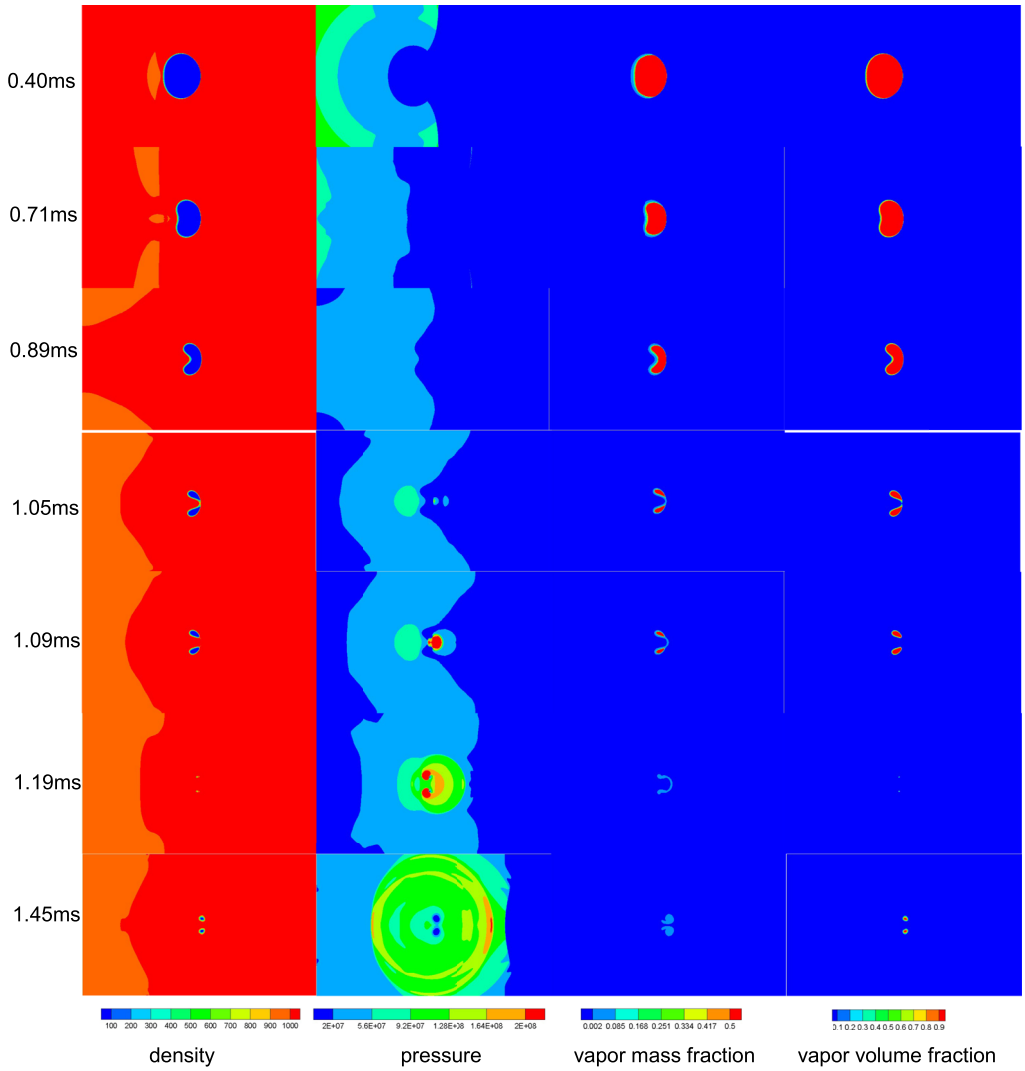

FIG. 9. Numerical results of the density, pressure, vapor mass, and volume fraction at different times t = 0.40, 0.71, 0.89, 1.05, 1.09, 1.19, and 1.45 ms.

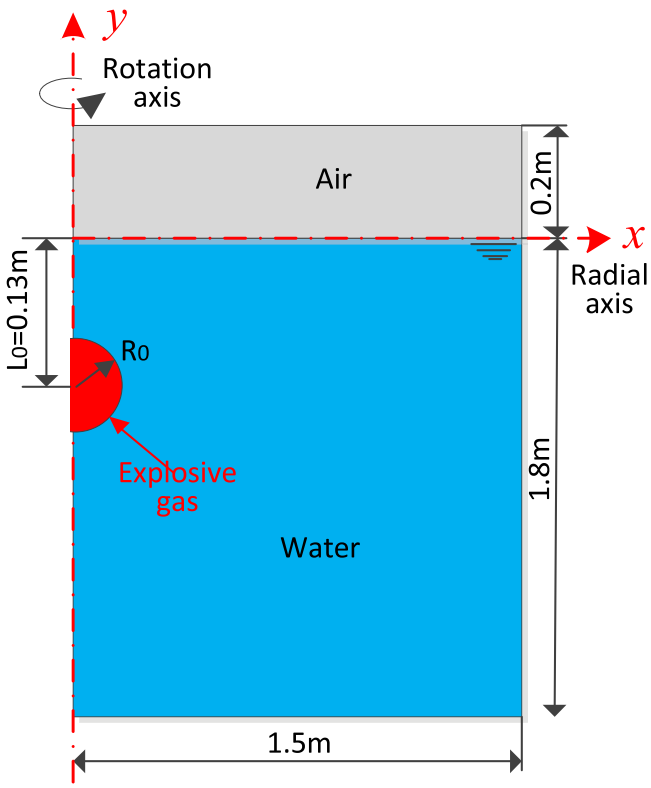

FIG. 10. Schematic of underwater explosion near a free surface.

boundary condition is applied on the other three boundaries. A highly compressed spherical explosive gas is located at $(x, y) = (0, -0.13)$ m, and the free surface is located at $y = 0$ m. With reference to the Geer–Hunter model[39] and our numerical experience, the initial explosion bubble produced after explosive initiation can be simplified using an equivalent detonation model. The initial static bubble has a radius of $R_0 = 0.01$ m, and its density and pressure are 1606 kg/m^3 and 10^9 Pa, respectively. An ideal gas law is used for the explosion gases with $\gamma = 1.8$, and its molar mass is approximated by the TNT with $W = 227$ g/mol.

The initial condition is

$$(\rho, u, p, Y_1, Y_2, Y_3, Y_4) = \begin{cases} (1.18, 0, 10^5, 0, 10^{-9}, 0.999, 0) & \text{for } air, \\ (1054, 0, 10^5, 0.999\,9, 10^{-8}, 4.73 \times 10^{-7}, 0) & \text{for } water, \\ (1606, 0, 10^9, 0, 10^{-8}, 0, 0.999) & \text{for } gas. \end{cases} \tag{19}$$

The initial temperatures for explosive gas, air, and water are 1080, 295, and 295 K, respectively. Under this condition, the initial air and explosive gas are overheated and the water is saturated. In this test, we activate thermal and chemical relaxation (phase transition) for the liquid and vapor water phases. For comparison, we run a simulation with no phase transition, which allows us to highlight the effect of mass and heat transfer processes. The numerical results are provided by the contours of the density, pressure, vapor volume fraction, and cavitation domain (from top to bottom) at four different times $t = 0.103$, 0.168, 0.334, 0.500, and 0.666 ms (from left to right), as shown in Fig. 11. The coordinate range of

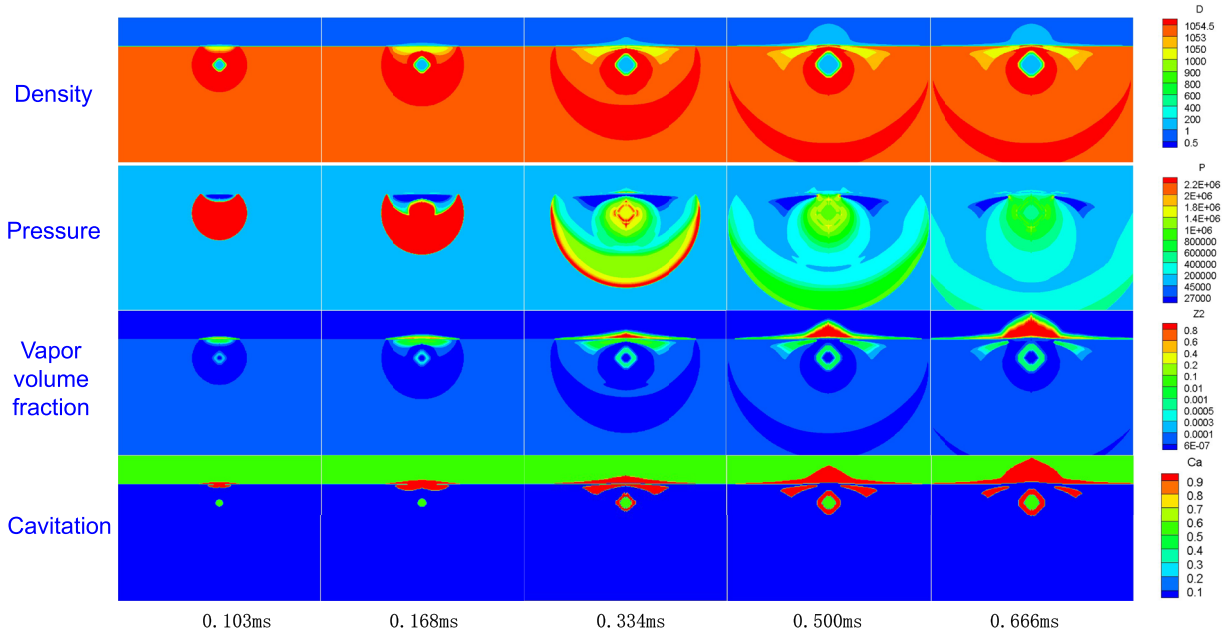

FIG. 11. Numerical results of the density, pressure, vapor volume fraction, and cavitation domain (from top to bottom) at five different times $t = 0.103$, 0.168, 0.334, 0.500, and 0.666 ms (from left to right). The black lines indicate the general location of the explosion bubble interface, and the black dotted lines denote the location of the initial free surface. The red region in the third column of frames represents the cavitation domain.

all the observation windows in Fig. 11 is [−0.7, 0.7] × [−0.8, 0.2] m^2. When the vapor volume fraction in a fluid element is greater than 0.5‰ ($\phi_2 > 0.5‰$), the element is marked as the red cavitation domain, as shown in Fig. 11. It can be observed that the rarefaction waves are reflected from the free surface and induce cavitation occurrence above and below the free surface at t = 0.103 ms. In this study, we refer to the cavitation in air above the water surface as the vapor cavity to distinguish it from the underwater cavitation. At t = 0168 ms, the rarefaction waves reach the explosion bubble interface, and shock waves are reflected from the interface. With the upward propagation of the reflected shock wave from the explosion bubble interface, the cavitation on the symmetry axis (y-axis) begins to collapse from the bottom to top, and the thickness of the cavitation on the y-axis starts to decrease, as shown at t = 0.334 ms. However, the rarefaction wave region caused by the reflection of the initial explosion shock wave on the free surface gradually expands, consequently inducing new cavitation domain occurrence in the far area on both sides of the y-axis. With the gradual collapse of the cavitation in the region near the y-axis and the continuous formation of the cavitation in the far area from the y-axis, the entire cavitation under the free surface in the 2D axisymmetric coordinate system forms into the shape of a vortex ring, as shown in Fig. 11. To some extent, the existence of the explosion bubble induces the collapse of cavitation. Because the bubble interface can reflect the rarefaction wave propagating from the free surface into a shock wave, the cavitation domain is compressed and subsequently induced to collapse. For the case of deep-water nuclear explosion, the cavitation domain is substantial because of the long loading time of the released shock wave. Meanwhile, the explosion bubble interface is far from the water surface, and it takes a long time for the cavitation to collapse, resulting in a possible harm of the surrounding ships.

As shown in Fig. 12, we compare the experimental and numerical results of the changes in the cavitation domain. The coordinate range of all the numerical frames in Fig. 12 is [−0.4, 0.4] × [−0.68, 0.2] m^2, which is similar to the window size of the experimental frames. The marks from 01 to 05 in the lower left corner of the

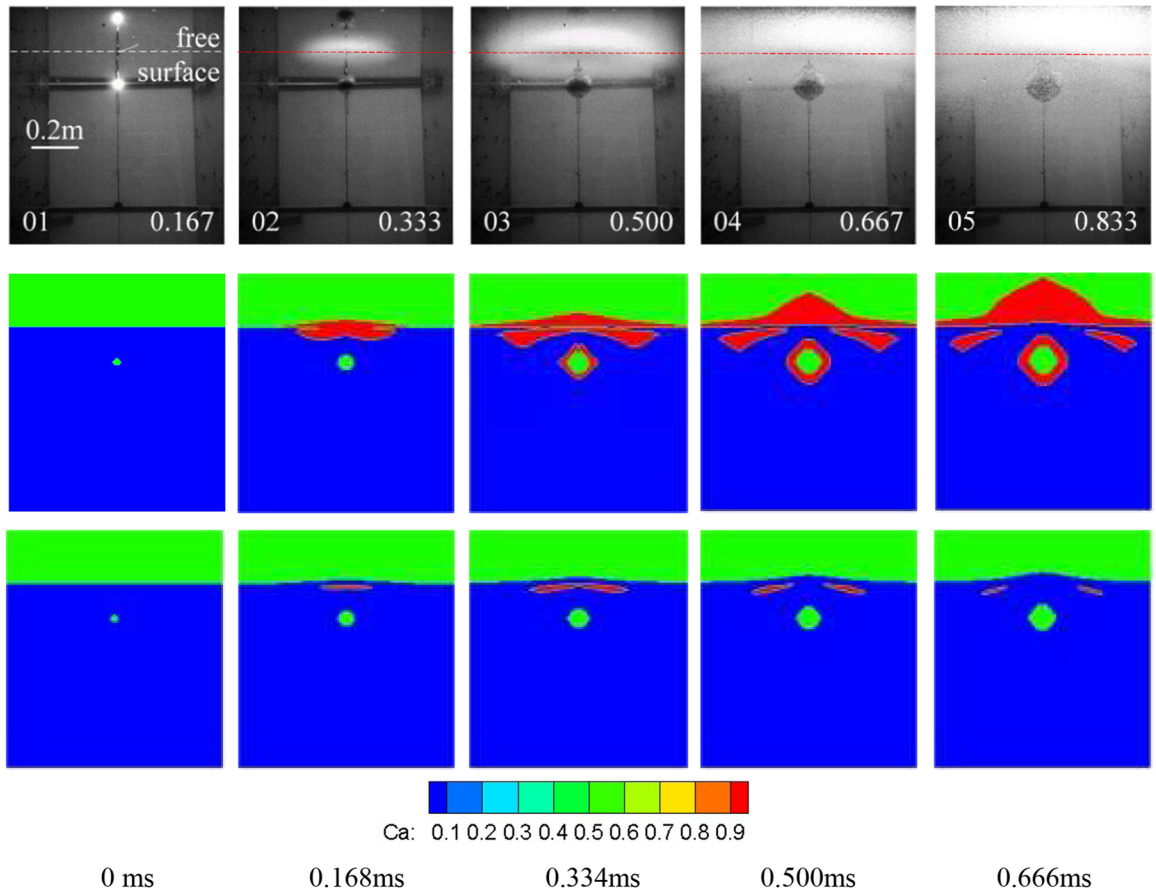

FIG. 12. Comparison of experimental and numerical results on the cavitation domain. Experimental frames (top row plots) and the cavitation domain with phase transition (middle row plots) and without phase transition (bottom row plots) are shown at times t = 0, 0.168, 0.334, 0.500, and 0.666 ms. The red and blue regions indicate the cavitation and liquid water domains, respectively, and the green regions indicate the air domain above the free surface and explosion gas. The black dotted lines indicate the initial free surface in experimental frames.

experimental frames (top row plots) denote the serial number of the photograph recorded by the camera, while the decimals on the right denote the corresponding time (in ms). The numerical results of the cavitation domain with and without phase transition are shown in the middle and bottom row plots, respectively. It can be observed that the numerical results with phase transition show excellent agreement with the experimental results. A vortex band composed of a large number of tiny cavitation bubbles can be observed, and the motion of the cavitation domain is similar to the numerical results with phase transition. However, the cavitation domain obtained by the model without phase transition is obviously smaller than the experimental results.

Figure 13 shows the numerical pressure time–history curves for two points on the y-axis with and without phase transition. The axis $y = 0$ m represents the initial position of the free surface. It can be observed that although the shock wave first reaches the measuring point ($y = -5.0$ cm) far from the free surface, it produces a relatively late cavitation. This is because the rarefaction waves begin to propagate downward from the free surface, which is consistent with the pressure propagation process in Fig. 11. We can also observe that the cavitation on the measuring point ($y = -5.0$ cm) is the first to collapse because the shock wave reflected by the rarefaction waves on the explosion bubble interface first reaches this point. The phase transition has practically no effect on the early shock wave stage. However, it has a great influence on the cavitation collapse stage. Relatively, the collapse pressure at the measuring point of $y = -2.5$ cm closer to the free surface fluctuates violently and the peak collapsing pressure is high under the condition of phase transition. The phase transition has little effect on the measuring point of $y = -5.0$ cm on the entire pressure stage, which is due to the short duration of cavitation. Therefore, the longer the duration of cavitation, the more obvious the phase transition effect. This is because the phase

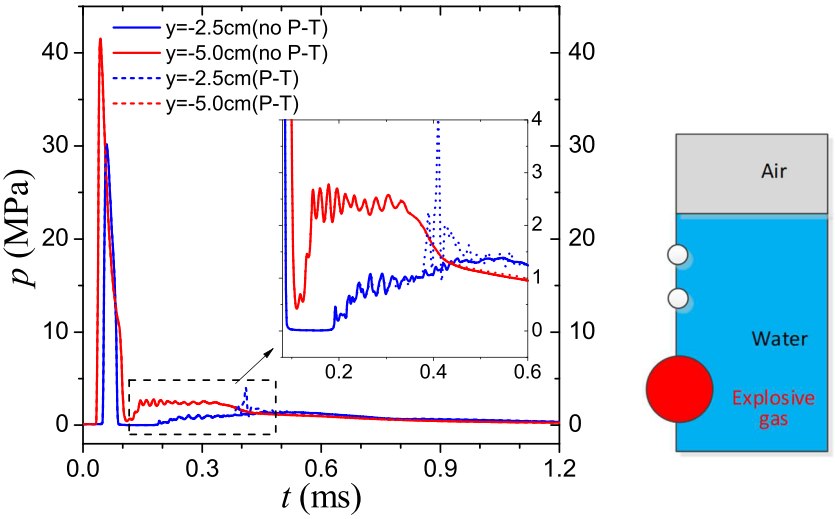

FIG. 13. Numerical results of the pressure time–history curves for two points on the axisymmetric axis (left) with and without phase transition and the schematic diagram of measuring points (right).

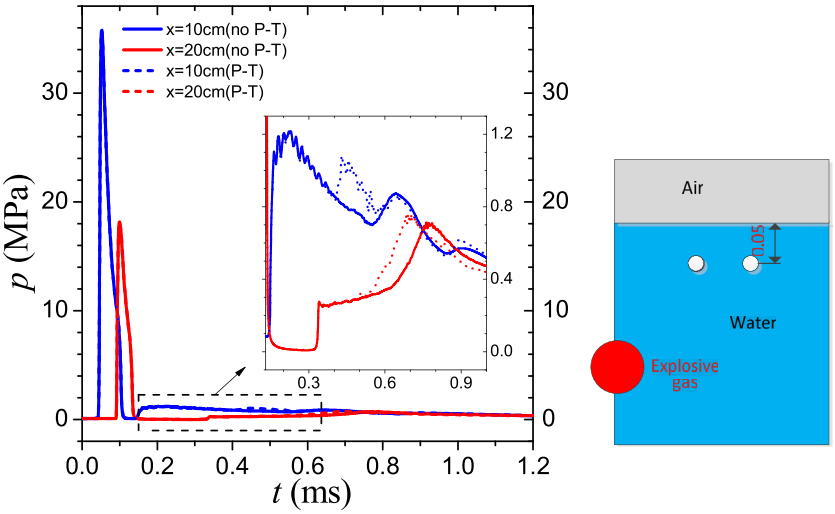

FIG. 14. Numerical results of the pressure time–history curves for two points at a depth of 0.05 m with and without phase transition (left) and the schematic diagram of measuring points (right).

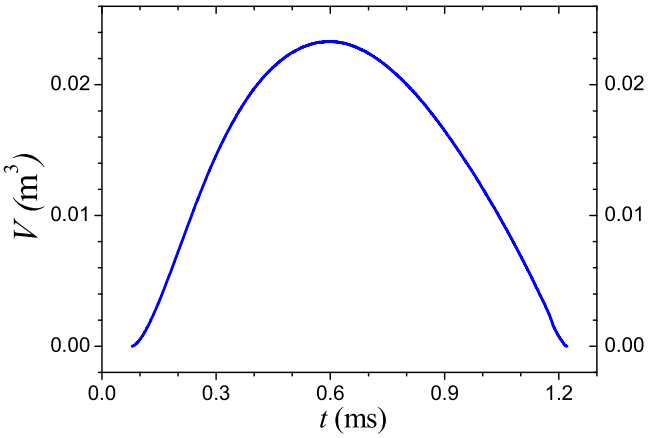

FIG. 15. Time history of total volume of the cavitation domain underwater.

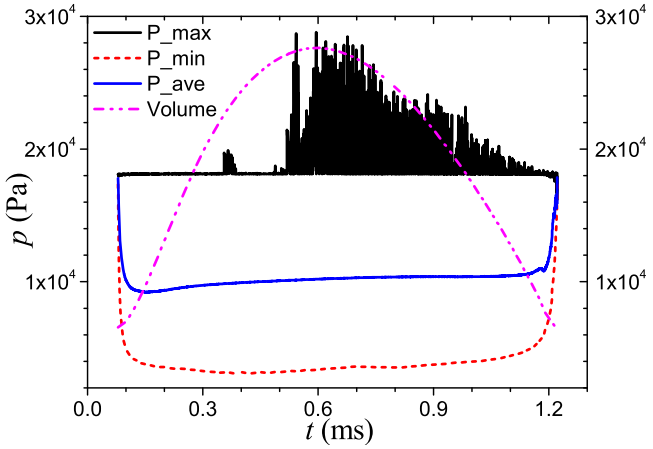

FIG. 17. Time history of the maximum, minimum, and average pressure changes in the cavitation domain.

transition process is closely related to the mass and heat transfer between the liquid and vapor phases. Figure 14 shows the numerical pressure time–history curves for two points at a depth of 0.05 m with and without phase transition. It can be observed that the phase transition has a level of influence on the two measuring points in the cavitation collapse stage. However, it has no effect on the early shock wave stage.

Figure 15 shows the time history curve of the total volume of the cavitation domain. It can be seen that the expansion process and contraction process times of the total volume of cavitation are approximate, and the entire cavitation movement cycle is ~1.14 ms. For the temperature in the cavitation domain, Fig. 16 reveals the time history curves of maximum, minimum, and average temperature changes in the cavitation domain similar to those in Fig. 12. It can be observed that when the cavitation domain expands to the maximum volume, the maximum and minimum temperatures in the cavitation domain are 309.7 and 283.7 K, respectively; however, the average temperature in the cavitation domain is basically constant at 294.6 K, which is equivalent to room temperature.

Figure 17 shows the time history curves of maximum, minimum, and average pressure changes in the cavitation domain. It can be seen that the maximum pressure is maintained at ~0.018 MPa most of the time in the expansion stage, while it mainly oscillates above 0.018 MPa in the contraction stage, and the maximum value reaches 0.029 MPa. The minimum pressure in the cavitation domain frequently changes gently in the middle in the range of 3200–4800 Pa. However, the change gradient is significant in the initial generation and final collapse stage of cavitation. The variation range of volume average pressures in the cavitation domain is 9000–18 000 Pa, and its variation trend is consistent with that of minimum pressure. It can be observed that the pressure in the cavitation domain changes in the saturated state and has the

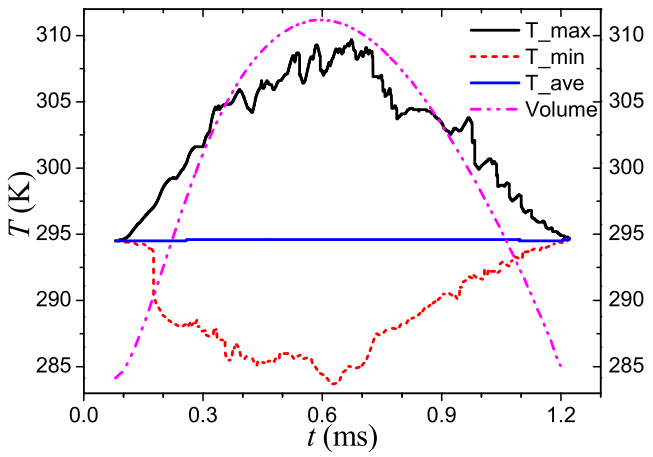

FIG. 16. Time history of the maximum, minimum, and average temperature changes in the cavitation domain.

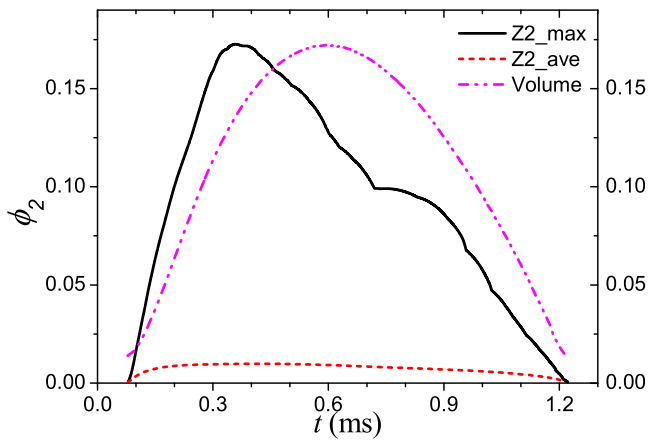

FIG. 18. Time history of the maximum and average vapor volume fractions in the cavitation domain.

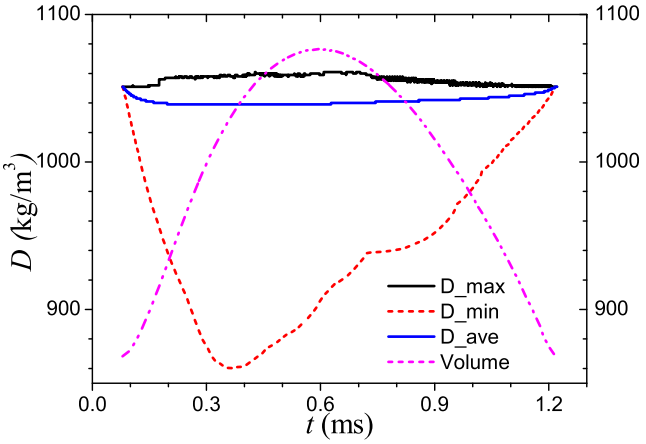

FIG. 19. Time history of the maximum, minimum, and average densities in the cavitation domain.

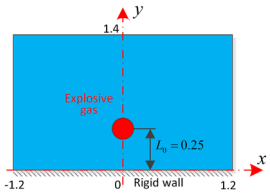

FIG. 20. Schematic of underwater explosion near a rigid wall.

characteristics of uneven distribution and large variation gradient. Meanwhile, the variation range of internal temperatures is 283.7–309.7 K as shown in Fig. 16, which indicates an apparent phase transition in the cavitation domain.

Figure 18 reveals the time history curve of the maximum and average variation of the vapor phase volume fraction in the cavitation domain, and the minimum value is 0.5‰. It can be seen from the diagram that the volume fraction of the vapor phase in the cavitation domain is 0.5‰–17.3%, and its peak does not appear at the time when the cavitation volume expands to the maximum volume. Although the maximum volume fraction of the vapor phase in the entire process of cavitation is not low, the average value of the whole volume in the cavitation domain varies from 0.5‰ to 1.0%, indicating that the average content of steam is relatively low. This is consistent with the "cloud cavitation" observed in the previous experiments shown in Fig. 12. Figure 19 shows the time history curve of the maximum, minimum, and average variations of density in the cavitation domain. It can be observed that the maximum density in the cavitation domain varies from 1051 to 1061 kg/m^3, and the average density ranges from 1039 to 1051 kg/m^3. Combined with Fig. 18, it can be observed that the content of the vapor phase in the cavitation domain is generally diminutive, and its density is similar to that of liquid phase water.

2. Underwater explosion cavitation near a rigid wall

When the high-pressure explosive gas is close to the structure in underwater, the local cavitation will appear in the fluid due to the structural motion and the effect of the explosion bubble boundary. In this chapter, the motion effect of the structure is ignored, and the structure is simplified to a fixed solid wall. A two-dimensional

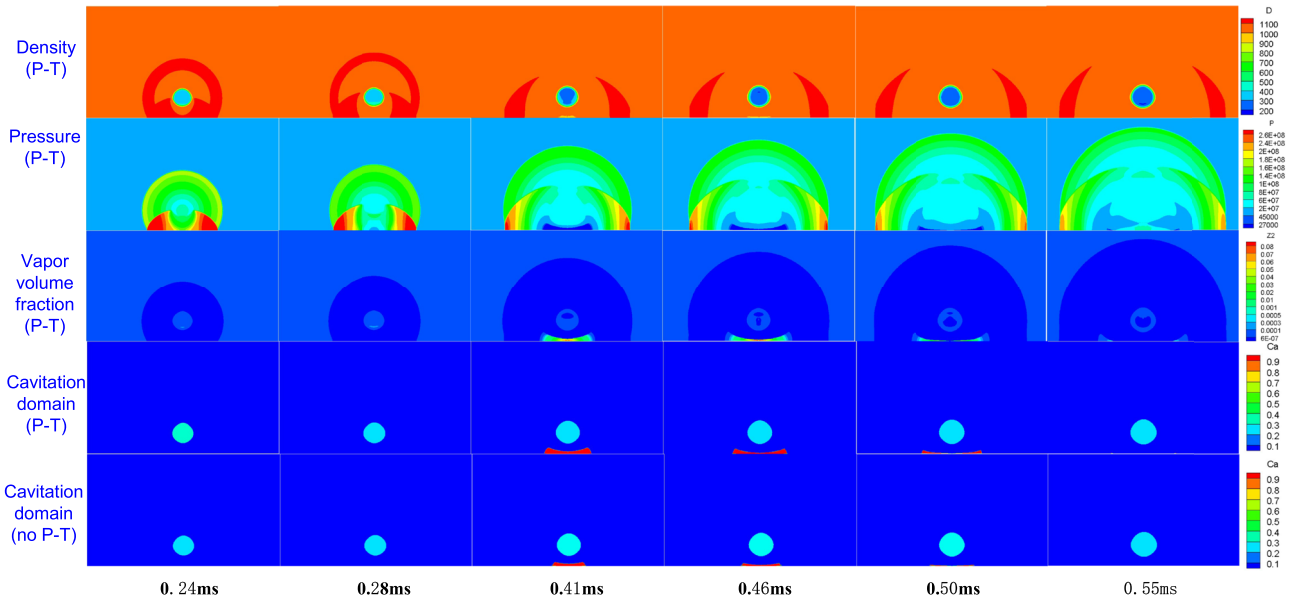

FIG. 21. Numerical results of the density, pressure, vapor volume fraction, and cavitation domain with and without P-T (from top to bottom) at different times t = 0.24, 0.28, 0.41, 0.46, 0.50, and 0.55 ms (from left to right). The red areas represent the cavitation domain in the fourth and fifth row contours.

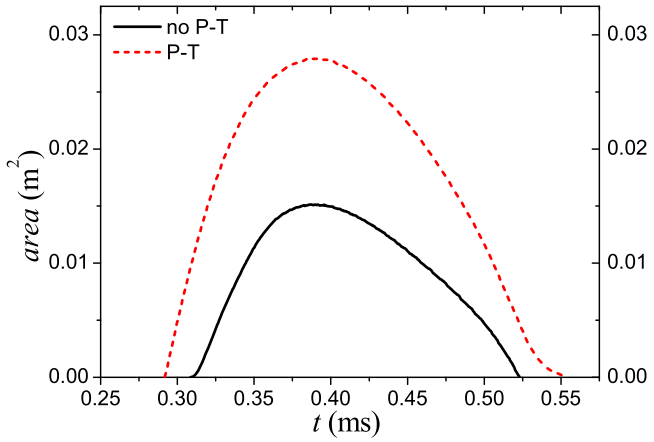

FIG. 22. Comparison of the evolution process of the cavitation domain area with and without phase transition conditions.

symmetric model is used as shown in Fig. 20. The cylindrical explosive gas has a radius of $R_0 = 0.05$ m and is located at the distance of $L_0 = 0.25$ m from the lower rigid wall. The rectangular computational domain for this problem is $\Omega = [0, 1.2] \times [0, 1.4]$ m^2, which is discretized by 600 × 700 grids. The initial condition is

$$(\rho, u, p, Y_1, Y_2, Y_3, Y_4) = \begin{cases} (1606, 0, 10^9, 0, 10^{-6}, 0, 0) & \text{for } gas, \\ (1054, 0, 10^5, 0.999\,9, 10^{-8}, 4.73 \times 10^{-7}, 0) & \text{for } water. \end{cases} \tag{20}$$

The numerical results are provided by the contours of the pressure, vapor volume fraction, and cavitation domain with and without phase transition (P-T) (from left to right) at six different times $t = 0.24$, 0.28, 0.41, 0.46, 0.50, and 0.55 ms (from top to bottom) as shown in Fig. 21. The red regions represent the cavitation domain in the third and fourth columns of plots. The identification criterion of the cavitation domain is the same as that in Figs. 11 and 12. The coordinate range of all the observation windows in Fig. 21 is the whole domain as shown in Fig. 20. It can be observed from the pressure plots that the compressed wave reflected from the lower rigid wall has reached an explosion bubble interface, and the rarefaction wave has been reflected to the lower water domain at 0.24 ms. However, there is no obvious cavitation domain in water, which is due to the fact that the reflected rarefaction wave intensity is not strong enough to cause the liquid phase in water to convert into a large amount of vapor phase. At 0.28 ms, the rarefaction wave has just reached the rigid wall. As more and more rarefaction waves are reflected on the rigid wall, the rarefaction waves near the wall are strengthened, and obvious cavitation regions gradually appear

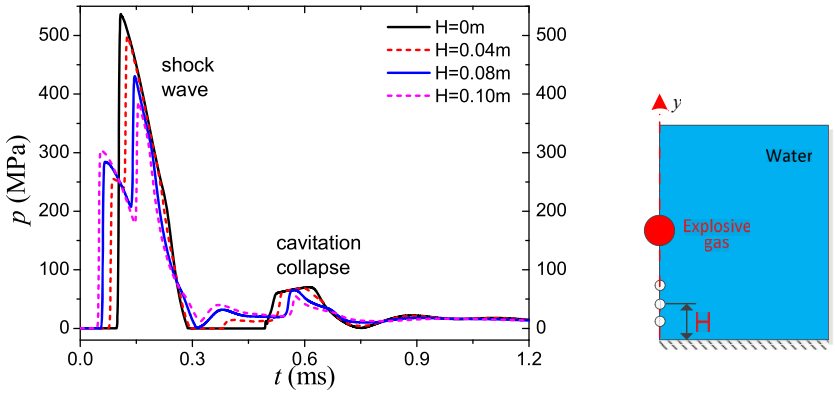

FIG. 23. Pressure time–history curves for different vertical distances from the rigid wall on the symmetric axis (left) and the schematic diagram of the measuring point location (right).

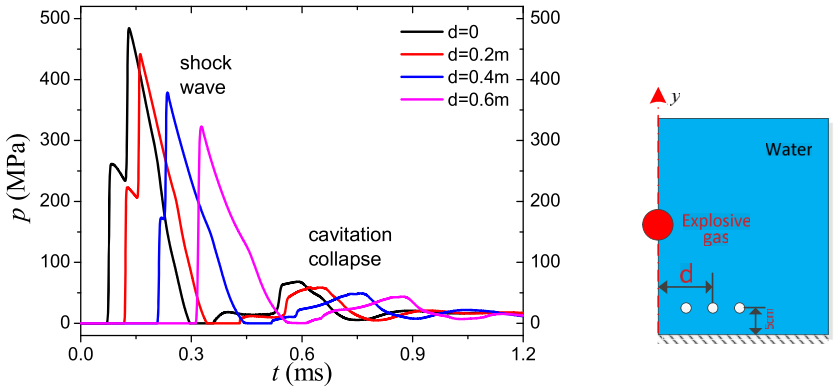

FIG. 24. Pressure time–history curves for different horizontal distances from explosive gas at a depth of 5 cm (left) and the schematic diagram of the measuring point location (right).

in water. The area of the cavitation domain reaches the maximum at about 0.41 ms. Since then, due to the movement of the explosion bubble and occurrence of the compressed wave from the reflection of the rarefaction wave at the explosion bubble interface, the cavitation domain in water gradually becomes smaller at 0.46 and 0.50 ms. The cavitation domain completely collapses at 0.55 ms as shown in Fig. 21. It can be observed from the cavitation domain contour plots that the range of the cavitation domain is obviously reduced under the condition of without phase transition. Figure 22 shows the comparison of the evolution process of the cavitation domain area. There are many differences in the starting time, duration, and maximum area of cavitation, which show that the phase transition has an important influence on the development of cavitation.

Figure 23 shows the pressure time–history curves for four points on the symmetric axis (y-axis). It can be observed that the point on the rigid wall (H = 0 cm) is the first to produce cavitation at t = 0.288 ms, which accords with the above conclusion that the rarefaction wave reflected from the explosion bubble interface for the first time cannot induce cavitation and needs to be further reflected and enhanced on the rigid wall. Figure 24 shows the pressure time–history curves for four points at a depth of 0.05 m. It can be observed that the nearer the point to the symmetric axis (y-axis), the earlier the cavitation occurs.

V. DISCUSSION AND CONCLUSIONS

In this paper, we adopted a numerical model for compressible multiphase flows based on the phase transition[18] and extended the model to the application in underwater explosion cavitation. The multiphase equations are solved using a simple fractional step approach that contains hyperbolic and relaxation steps. A monotonic mixture speed of sound is adopted using the HLLC approximate Riemann solver. The numerical model is first tested in several 1D shock tube and 2D vapor bubble examples and subsequently extended to underwater explosion cavitation near a free surface and rigid wall. The following conclusions are drawn:

(1) The Allaire speed is the most preferred mixture sound speed near the discontinuity in multiphase fluids based on the numerical results, while the Wood speed is non-monotonous, and the frozen speed is too ideal for an actual process. Therefore, the Allaire speed is adopted in this study.
(2) Generally, the phase transition model is sensitive to the vapor mass fraction. Therefore, the discontinuous problems with different vapor mass fractions are simulated in 1D shock tube tests. The numerical results show that the phase transition model in this study presents superior adaptability and can accurately capture the vaporization phenomenon in the propagation of shock waves and the condensation phenomenon in the propagation of rarefaction waves.
(3) It can be observed that the phase transition in thermodynamics shows great potential in the study of underwater explosion cavitation. For the underwater explosion near a free surface, the numerical results show that the rarefaction wave reflected by the initial explosion shock wave on the free surface leads to the cavitation creation, while the compression wave reflected from the upper interface of the explosion bubble causes cavitation collapse. It can also be observed that a vortex band composed of a substantial number of tiny cavitation bubbles in numerical results with phase transition is consistent with the experimental results in underwater explosion near a free surface.
(4) For the underwater explosion near a rigid wall, it can be concluded that the direct rarefaction wave reflected directly for the first time cannot induce cavitation creation. The cavitation begins to occur only when the direct rarefaction wave is reflected again on the rigid wall and further strengthened. The cavitation begins to collapse when the compression wave reflected from the upper interface of the explosion bubble impacts the cavitation domain.

Although the phase transition model in this study provides an effective method for underwater explosion cavitation, some limitations do exist. The interactions between the explosion gas, water, air, and structures are complex, and numerical results need to be further verified by experiments. In addition to the phase transition model, we aim to develop a solution that can alleviate the challenges present in the current research field. These progressions will be introduced in the future.

ACKNOWLEDGMENTS

The authors are grateful for useful discussions with Professor Richard Saurel. The authors would also like to thank the reviewers for their insightful comments.

AUTHOR DECLARATIONS

Conflict of Interest

The authors have no conflicts to disclose.

DATA AVAILABILITY

The data that support the findings of this study are available from the corresponding author upon reasonable request.

REFERENCES

[1] R. H. Cole, *Underwater Explosion*, Princeton University Press, Princeton, NJ, pp. 3–8 (1948).
[2] J. H. Liu, "Theory and its applications of ship dynamic responses to non-contact underwater explosions," China Ship Scientific Research Center, Ph.D. thesis, 2002, pp. 5–8.
[3] J. R. Qin, S. T. J. Yu, and M. C. Lai, "Direct calculations of cavitating flows in fuel delivery pipe by the space-time CE/SE method," SAE Trans. **108**, 1720–1725 (1999).
[4] T. G. Liu, B. C. Khoo, and W. F. Xie, "Isentropic one-fluid modelling of unsteady cavitating flow," J. Comput. Phys. **201**, 80–108 (2004).
[5] J. E. van Aanhold, G. J. Meijer, and P. P. M. Lemmen, "Underwater shock response analysis on a floating vessel," Shock Vib. **5**, 53–59 (1998).
[6] H. S. Tang and D. Huang, "A second-order accurate capturing scheme for 1D inviscid flows of gas and water with vacuum zones," J. Comput. Phys. **128**, 301–318 (1996).
[7] D. P. Schmidt, C. J. Rutland, and M. L. Corradini, "A fully compressible, two-dimensional model of small, high speed, cavitating nozzles," Atomization Sprays **9**, 255–276 (1999).
[8] W. F. Xie, T. G. Liu, and B. C. Khoo, "Application of a one-fluid model for large scale homogeneous unsteady cavitation: The modified Schmidt model," Comput. Fluids **35**, 1177–1192 (2006).

[9]A. Daramizadeh and M. R. Ansari, "Numerical simulation of underwater explosion near air-water free surface using a five-equation reduced model," Ocean Eng. **110**, 25–35 (2015).
[10]O. Le Métayer, J. Massoni, and R. Saurel, "Elaborating equations of state of a liquid and its vapor for two-phase flow models," Int. J. Therm. Sci. **43**, 265–276 (2004).
[11]O. Le Métayer, J. Massoni, and R. Saurel, "Modeling evaporation fronts with reactive Riemann solvers," J. Comput. Phys. **205**, 567–610 (2005).
[12]O. Le Métayer, J. Massoni, and R. Saurel, "Dynamic relaxation processes in compressible multiphase flows. Application to evaporation phenomena," ESAIM Proc. **40**, 103–123 (2013).
[13]R. Saurel, F. Petitpas, and R. Abgrall, "Modelling phase transition in metastable liquids: Application to cavitating and flashing flows," J. Fluid Mech. **607**, 313–350 (2008).
[14]M. Pelanti and K.-M. Shyue, "A mixture-energy-consistent six-equation two-phase numerical model for fluid with interfaces, cavitation and evaporation waves," J. Comput. Phys. **259**, 331–357 (2014).
[15]A. Zein, M. Hantke, and G. Warnecke, "Modeling phase transition for compressible two-phase flows applied to metastable liquids," J. Comput. Phys. **229**, 2964–2998 (2010).
[16]M. Pelanti and K.-M. Shyue, "A numerical model for multiphase liquid-vapor-gas flows with interfaces and cavitation," Int. J. Multiphase Flow **113**, 208–230 (2019).
[17]A. Chiapolino, P. Boivin, and R. Saurel, "A simple phase transition relaxation solver for liquid–vapor flows," Int. J. Numer. Methods Fluids **83**(7), 583–605 (2016).
[18]A. Chiapolino, P. Boivin, and R. Saurel, "A simple and fast phase transition relaxation solver for compressible multicomponent two-phase flows," Comput. Fluids **150**, 31–45 (2017).
[19]J. Zhang, "A simple and effective five-equation two-phase numerical model for liquid-vapor phase transition in cavitating flows," Int. J. Multiphase Flow **132**, 103417 (2020).
[20]O. Le Métayer and R. Saurel, "The Noble-Abel stiffened-gas equation of state," Phys. Fluids **28**, 046102 (2016).
[21]R. Saurel, P. Boivin, and O. Le Métayer, "A general formulation for cavitating, boiling and evaporating flows," Comput. Fluids **128**, 53–64 (2016).
[22]A. Akturk, "Two-dimensional finite volume weighted essentially non-osciliatory Euler schemes with different flux algorithms," M.S. thesis, Middle East Technical University, 2005.
[23]E. F. Toro, *Riemann Solvers and Numerical Methods for Fluid Dynamics* (Springer, Berlin, 2009).
[24]A. B. Wood, *A Textbook of Sound* (G. Bell and Sons Ltd., London, 1930).
[25]A. K. Kapila, R. Menikoff, J. B. Bdzil, S. F. Son, and D. S. Stewart, "Two-phase modeling of deflagration-to-detonation transition in granular materials: Reduced equations," Phys. Fluids **13**, 3002–3024 (2001).
[26]A. Murrone and H. Guillard, "A five equation reduced model for compressible two-phase flow problems," J. Comput. Phys. **202**, 664–698 (2005).
[27]A. Tiwari, J. B. Freund, and C. Pantano, "A diffuse interface model with immiscibility preservation," J. Comput. Phys. **252**, 290–309 (2013).
[28]R. Saurel, F. Petitpas, and R. A. Berry, "Simple and efficient relaxation methods for interfaces separating compressible fluids, cavitating flows and shocks in multiphase mixture," J. Comput. Phys. **228**, 1678–1712 (2009).
[29]G. Allaire, S. Clerc, and S. Kokh, "A five-equation model for the simulation of interfaces between compressible fluids," J. Comput. Phys. **181**, 577–616 (2002).
[30]G. Perigaud and R. Saurel, "A compressible flow model with capillary effects," J. Comput. Phys. **209**, 139–178 (2005).
[31]V. K. Kedrinskii, *Hydrodynamics of Explosion: Experiments and Models* (Springer, 2005), pp. 125–136.
[32]R. K. Shukla, C. Pantano, and J. B. Freund, "An interface capturing method for the simulation of multi-phase compressible flows," J. Comput. Phys. **229**, 7411–7439 (2010).
[33]E. Johnsen and T. Colonius, "Implementation of WENO schemes in compressible multicomponent flow problems," J. Comput. Phys. **219**, 715–732 (2006).
[34]J. Yu, G.-z. Liu, J. Wang, and H.-k. Wang, "An effective method for modeling the load of bubble jet in underwater explosion near the wall," Ocean Eng. **220**, 108408 (2021).
[35]A. H. Kennard, "The effect of pressure wave on a plate or diaphragm," Comput. Underwater Explos. Res. **3**, 11–64 (1944).
[36]H. N. V. Temperley, "Theoretical investigation of cavitation phenomena occurring when an underwater pressure pulse is incident on a yielding surface," Underwater Explos. Res. **3**, 260–268 (1950).
[37]C. F. Hung, P. Y. Hsu, and J. J. Hwang-Fuu, "Elastic shock response of an air-backed plate to underwater explosion," Int. J. Impact Eng. **31**, 151–168 (2005).
[38]P. Cui, A. M. Zhang, and S. P. Wang, "Small-charge underwater explosion bubble experiments under various boundary conditions," Phys. Fluids **28**, 117103 (2016).
[39]T. L. Geers, "Doubly asymptotic approximations for transient motions of submerged structures," J. Acoust. Soc. Am. **64**, 1500–1508 (1987).
[40]S. F. Davis, "Simplified second-order Godunov-type methods," SIAM J. Sci. Stat. Comput. **9**, 445–473 (1988).
[41]V. K. Kedrinskill, *Hydrodynamics of Explosion: Experiments and Models*, High-Pressure Shock Compression of Condensed Matter (Springer-Verlag, Berlin, Heidelberg, 2005), pp. 223–233.